Reducing Systematic Uncertainty in Computed Redox Potentials for Aqueous Transition-Metal-Substituted Polyoxotungstates

Jake A. Thompson, Rebeca González-Cabaleiro,* and Laia Vilà-Nadal*

ACCESS | Metrics & More | Article Recommendations | SI Supporting Information

ABSTRACT: Polyoxometalates have attracted significant interest owing to their structural diversity, redox stability, and functionality at the nanoscale. In this work, density functional theory calculations have been employed to systematically study the accuracy of various exchange–correlation functionals in reproducing experimental redox potentials, U^0_{Red} in $[PW_{11}M(H_2O)O_{39}]^{q-}$ M = Mn(III/II), Fe(III/II), Co(III/II), and Ru(III/II). U^0_{Red} calculations for $[PW_{11}M(H_2O)O_{39}]^{q-}$ were calculated using a conductor-like screening model to neutralize the charge in the cluster. We explicitly located K^+ counterions which induced positive shifting of potentials by > 500 mV. This approximation improved the reproduction of redox potentials for $K_x[XW_{11}M(H_2O)O_{39}]^{q-x}$ M = Mn(III/II)/Co(III/II). However, uncertainties in U^0_{Red} for $K_x[PW_{11}M(H_2O)O_{39}]^{q-x}$ M = Fe(III/II)/Ru(III/II) were observed because of the over-stabilization of the ion-pairs. Hybrid functionals exceeding 25% Hartree–Fock exchange are not recommended because of large uncertainties in ΔU^0_{Red} attributed to exaggerated proximity of the ion-pairs. Our results emphasize that understanding the nature of the electrode and electrolyte environment is essential to obtain a reasonable agreement between theoretical and experimental results.
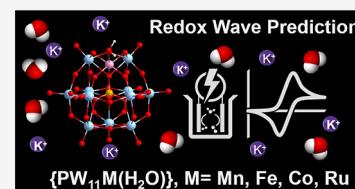
INTRODUCTION

Polyoxometalates (POMs) are a large group of discrete, polynuclear metal-oxo clusters comprising early transition-metal (addenda) and oxide atoms.[1–5] Addenda atoms are fully oxidized to d^0 electron configurations capable of forming various topologies employing $\{MO_x\}$ as the principal building block.[1–5] Poly-oxo clusters are formed from the acidification of aqueous molybdate or tungstate oxoanions.[6,7] Partial hydrolysis of poly-oxo clusters, achieved through the controlled addition of base produces lacunary clusters. These complexes formally lose one or several M = O vertices and possess reactive cavities with high charge density around the defective region due to the negatively charged oxygen ligands.[8] The defective region can react with transition-metal cations forming a new class of compounds, an example shown are mono-transition-metal-substituted polyoxotungstates, $[XW_{11}M(L)O_{39}]^{q-}$ (X = e.g., P(V), Si(IV), L = H_2O, DMSO, etc.)—see Table 1.[8] Conventionally, hexacoordinate transition-metals are introduced so the sixth coordination site are occupied by solvent ligands from the local environment—see Figure 1. These structures have attracted significant interest as single atom catalysts[9] in fields including water oxidation,[10,11] carbon dioxide reduction,[12,13] and nitrogen activation (Scheme 1).[14]

Early computational work on POMs have primarily focused on charged molecules using implicit solvation models.[38] In this regard, Poblet and co-workers reported the relative stability of rotational isomers of Keggin heteropolyanions, α/β-$[XM_{12}O_{40}]^{q-}$.[39] These calculations were performed using the local-density approximation functional coupled with Vosko–Wilk–Nusair parametrization, in the gas phase.[39] The enhanced stability of the α-$[XM_{12}O_{40}]^{q-}$ isomer was attributed to the

higher energy of the lowest occupied molecular orbital.[39] However, it was shown that four-times-reduced clusters $[PW_{12}O_{40}]^{7-}$ and $[SiMo_{12}O_{40}]^{8-}$ demonstrated enhanced stability (ca. 0.4 eV) toward the β-isomer.[39] Later, Zhang and co-workers emphasized the importance of implicit solvation for reproducing experimental geometries.[40] Several generalized gradient approximation (GGA) functionals were tested, in which Perdew–Burke–Ernzerhof (PBE) and Becke 1988 exchange and Perdew 86 (BP86) methods provided the closest description to the experimental geometries.[40] However, GGA functionals often poorly describe electron delocalization as previously reported by Poblet and co-workers.[41] Their work showed GGA functionals incorrectly localized an additional electron at the belt region in mono-substituted Wells–Dawson $[P_2W_{17}MO_{62}]^{q-}$ (M = V, Mo) anions.[41] On the other hand, employment of hybrid methods, such as B3LYP or M05 correctly localized the electron.[41] However, only B3LYP [20% Hartree–Fock (HF) exchange] gave the correct ordering and relative reduction energies with respect to experimental measurements.[41]

Quantum chemical calculations reproducing redox potentials in POMs have been reported without accounting for electrolyte environment and counterions, using implicit solvation models.
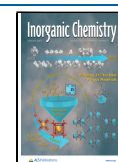
Table 1. Selected Mono-Transition-Metal-Substituted Keggin, $[PW_{11}M(L)O_{39}]^{q-}$, and Wells−Dawson, $[P_2W_{17}M(L)O_{61}]^{q-}$, Derivatives[a]

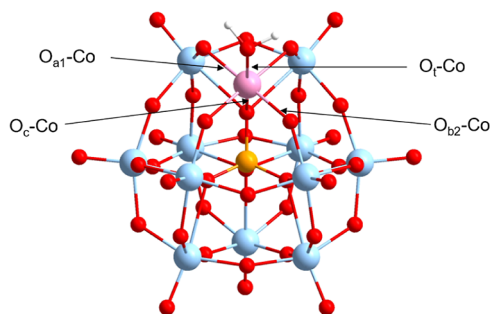| M, $[XW_{11}M(L)O_{39}]^{q-}$	XO_4, q = 4	XO_4, q = 5	XO_4, q = 6
Sc	PO_4[a,15]		
Cr	PO_4[a,16,17]	SiO_4[a,17,18]	
Ti		PO_4[b,19]	
Mn	PO_4[a,20]	PO_4[a,20] SiO_4[a,20] GeO_4[a,20]	BO_4[a,20] SiO_4[a,20] GeO_4[a,20]
Fe	AsO_4[a,21] PO_4[a,21]	PO_4[a,21] SiO_4[a,21] GeO_4[a,21]	SiO_4[a,21] GeO_4[a,21]
Co		PO_4[a,22]	SiO_4[a,23]
Ru	PO_4[a,c,24]	PO_4[a,25] SiO_4[a,c,26] GeO_4[a,c,27]	
Rh	PO_4[a,28]		SiO_4[d,29]
Ir	PO_4[a,30]		
Ni		PO_4[a,18]	SiO_4[a,31]
Cu		PO_4[a,18,20]	SiO_4[a,20] GeO_4[a,20]
Zn		PO_4[a,18]	
M, $[X_2W_{17}M(L)O_{61}]^{q-}$	XO_4, q = 6	XO_4, q = 7	XO_4, q = 8
Cr		PO_4[a,17]	
Ti			PO_4[e,32]
Mn		AsO_4[a,20] PO_4[a,20,33]	AsO_4[a,20] PO_4[a,20]
Fe		PO_4[a,33]	
Co			PO_4[a,33,34]
Ru		PO_4[a,b,35]	PO_4[a,b,35]
Ir	PO_4[a,36]		
Ni			PO_4[a,33]
Cu			AsO_4[a] PO_4[a,33]
Zn			PO_4[a,37]

[a]Note: [a]H_2O, [b]O, [c]C_2H_6OS, [d]Cl^-, [e]O_2.

Figure 1. Schematic representation for the cobalt(II)-substituted Keggin $[PW_{11}Co(H_2O)O_{39}]^{q-}$ anion. Colors corresponding to W = cyan, O = red, P = orange, and Co = pink.

Aparicio and co-workers computed the tungsten redox waves for mono-substituted Keggin, $[XMW_{11}O_{40}]^{q-}$ (M = W, Mo, V, Nb, and Ti) using a conductor−like screening mode.[42] This simplification produced large uncertainties in absolute reduction potential. However, shifts in potential with respect to the Keggin $[XM_{12}O_{40}]^{q-}$ anion were reproduced with corresponding experimental data.[42] Recently, Rösch and co-workers reported redox potentials for the tri-Mn-substituted Keggin in which counterions were explicitly located onto the surface of POM to neutralize the system.[43] The authors employed several exchange−correlation ($x−c$) functionals with the increase in contributions of HF exchange (0% PBE, 10% TPSSh, 20%

B3LYP, 25% PBE0) which produced redox potentials that increase (in that order) with the exact exchange.[43] The closest agreement with experimental literature was shown for the GGA−PBE functional attributed to fortuitous error cancellations. By contrast, hybrid exchange−functionals overestimated experimental potentials by 0.6−1.0 V.[43] This work was extended to include explicit treatment of water molecules derived from molecular dynamics simulations.[44] The inclusion of explicit solvation significantly improved computed redox potentials; however, its contributions were out-weighted by the choice of exchange−correlation functional.[44] In this work, optimal reproduction of experimental literature were obtained using the B3LYP method.[44] Recently, Falbo and Penfold reported the influence of the self-interaction error could be reduced by neutralizing the charged species by incorporating counterions into the system.[45] The authors reported excellent agreement, within 0.1 V of the experimental literature for the first redox wave in $Na_3[SiW_{12}O_{40}]$.[45]

In this work, we have performed systematic density functional theory (DFT) calculations to study the redox properties of $[PW_{11}M(H_2O)O_{39}]^{q-}$ M = Mn(III/II), Fe(III/II), Co(III/II), and Ru(III/II) and their potassium salts. For achieving adequate molecular geometries, we present a structural benchmark for the cobalt(II)-substituted Keggin against the crystallographic structure.[46] Thereafter, we explore the challenges in computing redox potentials and provide an insight into the geometric and electronic factors controlling it.

■ COMPUTATIONAL DETAILS

All computational results were obtained using the ARCHIE−WeSt high-performance computer based at the University of Strathclyde. DFT calculations were performed using the Amsterdam Modelling Suite (AMS 2020.1) package.[47] In this work, several classes of exchange−correlation ($x−c$) functionals were employed, which include (i) generalized gradient approximation (GGA); (ii) hybrid; and (iii) range-separated hybrid functionals. GGA functionals considered were as follows: (i) PBE;[48] (ii) Perdew−Wang (PW91);[49] and (iii) Becke 1988 exchange and Perdew 86 (BP86).[50,51] The hybrid $x−c$ functionals considered were as follows: (i) Becke, 3-parameter, Lee−Yang−Parr (B3LYP*,[52] B3LYP[53]); (ii) PBE0;[54] and (iii) Becke's half-and-half (BH&H).[55] Hybrid functionals were selected on their contributions of HF exchange (15% B3LYP*, 20% B3LYP, 25% PBE0, and 50% BH&H). The ωB97X method was selected as the range-separated hybrid functional.[56] We employed Slater basis sets comprising the following: (i) triple-ζ polarization (TZP); (ii) triple-ζ plus polarization (TZ2P); and (iii) quadruple-ζ plus polarization (QZ4P).[57,58] Relativistic corrections were included by means of the zeroth order regular approximation formalism.[59] The effects of aqueous solvent were approximated by using the conductor-like screening model, as implemented by AMS.[60] For open shell molecules, unrestricted Kohn−Sham (UKS) theory was implemented, while restricted Kohn−Sham (RKS) theory was employed for closed shell systems. All harmonic vibrational frequencies were calculated using PBE coupled with the TZP basis set. The calculation of Gibbs free energies for hybrid-optimized systems were corrected by using the zero-point energies and entropic components obtained from GGA−vibrational frequencies—see eq 1.0.

$$\Delta_r G = \Delta H + \Delta E_{ZPE} - T\Delta S \qquad (1.0)$$

Scheme 1. General Synthetic Strategy for Obtaining Co(II)-Substituted Keggin $[\alpha\text{-}PW_{11}Co(H_2O)O_{39}]^{5-}$ and Wells−Dawson $[\alpha_2\text{-}P_2W_{17}Co(H_2O)O_{61}]^{8-}$ Derivatives
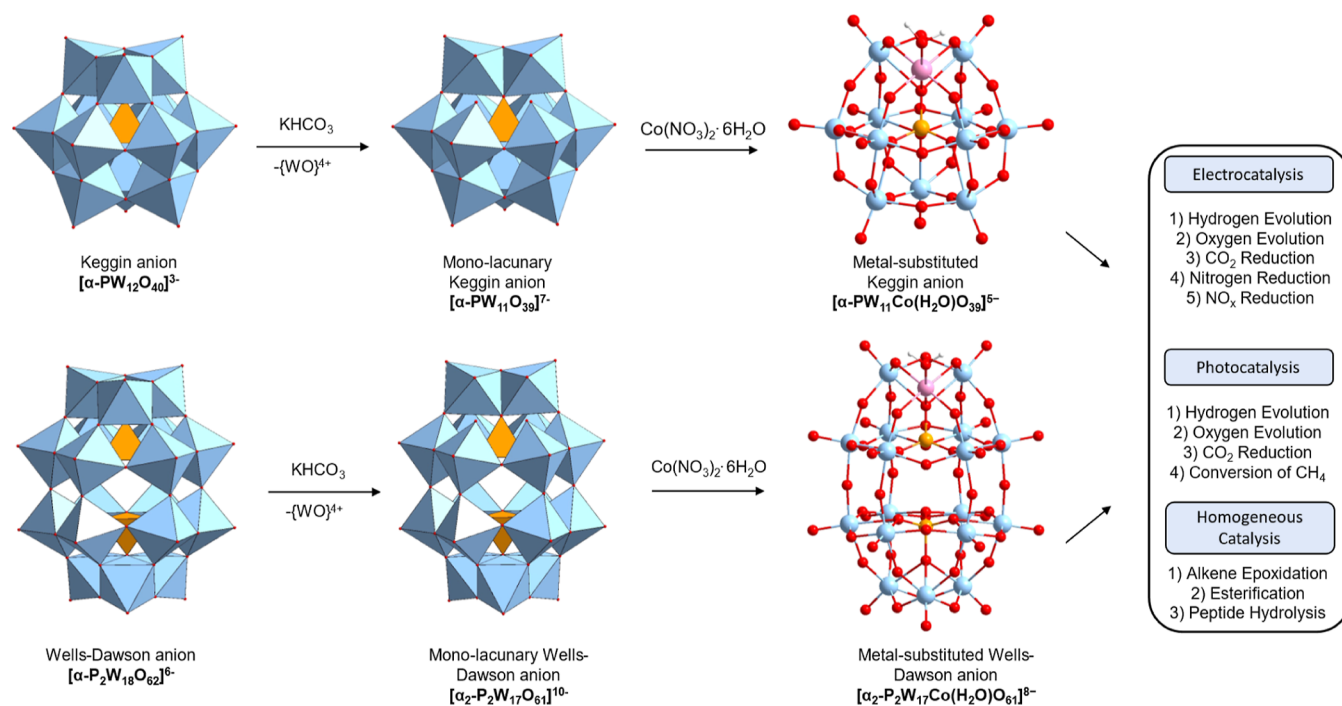
Herein, ΔH equates to the enthalpic component; ΔE_{ZPE} is the difference in zero-point energy, and $T\Delta S$ is the entropic component, under standard conditions, $T = 298.15$ K, $P = 1.0$ atm. The entropic and zero-point terms were computed using harmonic vibrational frequencies. Cramer and co-workers reported the free energy change for the standard hydrogen electrode (SHE) half-reaction $(1/2H_2 \rightarrow H^+ + e^-)$ equates to 4.24 eV.[61] This was used an external reference for all computed potentials.

To evaluate the discrepancy of the calculated versus crystallographic geometries, we employed mean absolute error (MAE), mean signed error (MSE), and standard deviation (STD) calculated using

$$MAE = \frac{1}{N}\sum_i |d_{calc,i} - d_{exp,i}| \tag{1.1}$$

$$MSE = \frac{1}{N}\sum_i (d_{calc,i} - d_{exp,i}) \tag{1.2}$$

$$STD = \sqrt{\frac{1}{N-1}\sum_i (MSE - (d_{calc,i} - d_{exp,i}))^2} \tag{1.3}$$

where d_{calc} and d_{exp} are the calculated and experimental bond distances, respectively.

RESULTS AND DISCUSSION

Structural Benchmark-Anionic Model. The selection of the exchange−correlation (x−c) functional and basis set and its ability to precisely describe the system of interest is a prerequisite for DFT studies. To assess the accuracy of x−c functionals and basis sets on the structural optimization of $[PW_{11}Co(H_2O)O_{39}]^{q-}$, MSE, and MAE were used to compare against the crystallographic structure, reported by Cavaleiro and co-workers.[46] Four types of oxygen atoms were examined: O_c

and O_t which correspond to the heteroatom−oxygen and terminal−oxygen atoms, while O_{a1} and O_{b2} denote bridging (equatorial) oxygens bound to the newly incorporated transition-metal—see Figure 1.

Figure 2a presents results for the selected structural parameters of $[PW_{11}Co(H_2O)O_{39}]^{q-}$ employed to assess the accuracy of applied functionals and basis sets. As is evident, equilibrium geometries in $[PW_{11}Co(H_2O)O_{39}]^{q-}$ were generally well described by all methods, rarely exceeding discrepancies of 0.18 Å. Figure 2b showed for systems with the increase in HF exchange, the magnitude of MSE progressively increased. Of particular note, hybrid functionals exceeding 20% HF exchange commenced underestimating equilibrium geometries, shown by MSE. For BH&H (50% exchange), MSE of ca. −0.05 Å was attributed to the underestimation of O_t−Co, O_{a1}−Co, and O_{b2}−Co by 0.236, 0.059, and 0.035 Å, respectively. Figure 2c reported calculated errors with respect to the selected bond. Herein, the primary source of error was the reproduction of the heteroatom−oxygen and terminal−oxygen bonds: O_c−Co and O_t−Co. The crystallographic structure of $[PW_{11}Co(H_2O)O_{39}]^{q-}$ illustrates the magnitude of O_t−Co surpasses O_c−Co, reporting distances of 2.321 and 2.079 Å, respectively.[46] However, our models have inverted this observation, in which the magnitude of O_c−Co exceeds O_t−Co. Across all methods, the equatorial distances were accurately described with computed errors rarely exceeding 0.02 Å. The equatorial parameters were insensitive across all applied functionals and basis sets, reporting a range of 0.059 and 0.085 Å for O_{a1}−Co and O_{b2}−Co, respectively.

The electronic structure of a fully oxidized POM consists of two identifiable bands: (i) an oxo-band comprising occupied oxo-ligands; (ii) and a metallic band encompassing unoccupied addenda orbitals. Figure 3 depicts the frontier molecular orbitals of $[PW_{11}M(H_2O)O_{39}]^{q-}$ anions, optimized using the PBE/TZP level of theory. Herein, orbitals associated with the newly
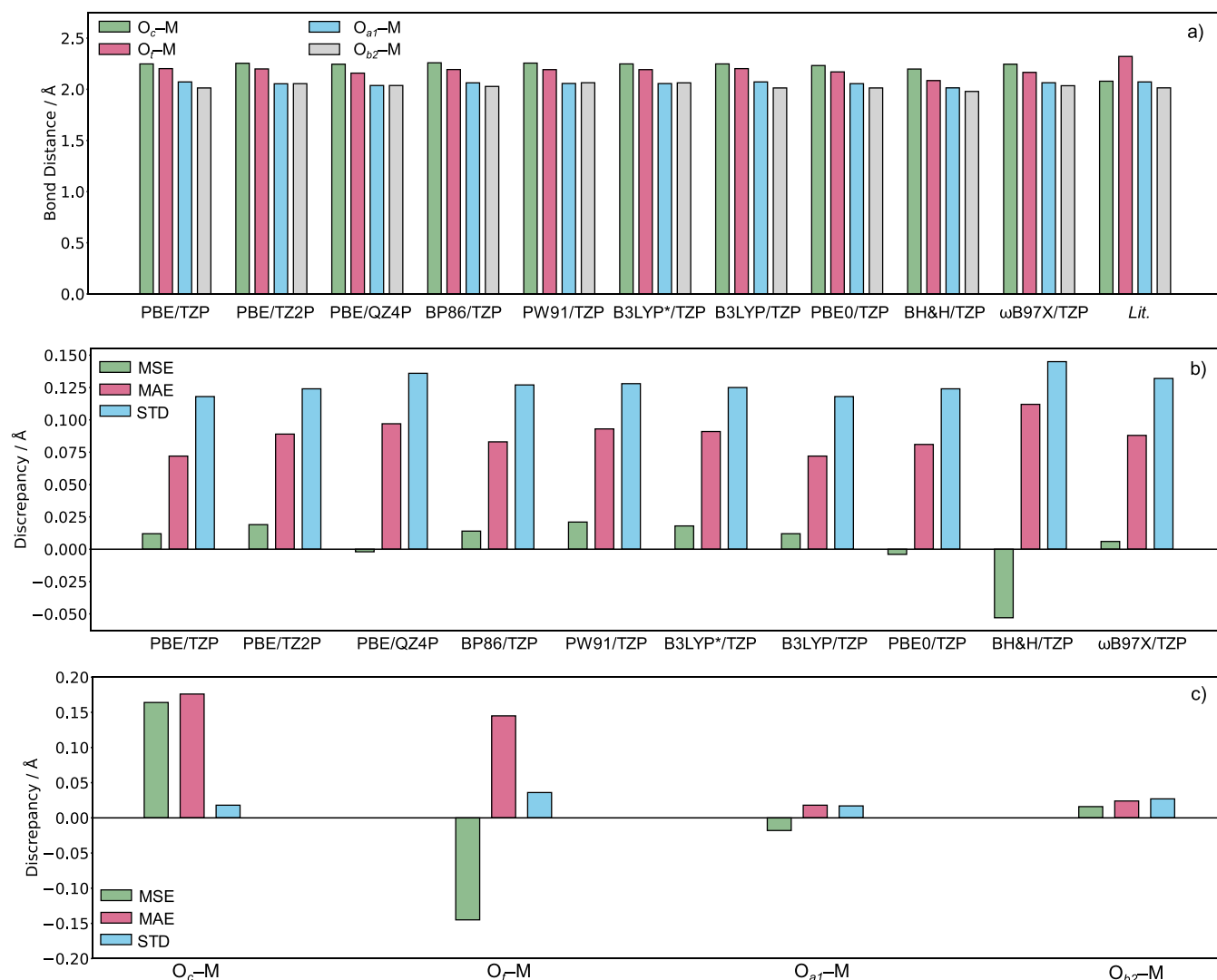
Figure 2. (a) Selected structural parameters for the cobalt(II)-substituted Keggin $[PW_{11}Co(H_2O)O_{39}]^{q-}$ anion referenced against the crystallographic structure taken from Cavaleiro and co-workers.[46] (b) MSE, MAE, and STD calculated for all applied functionals and basis sets. (c) MSE, MAE, and STD calculated for four types of metal−oxygen interactions. All bond distances are reported in Å.

incorporated transition-metal are inserted between the occupied oxo and unoccupied addenda band.

Cyclic voltammetric experiments have explored the redox behavior for $[PW_{11}M(H_2O)O_{39}]^{q-}$ M = Mn(III/II),[20] Fe(III/II),[21] Co(III/II),[23,24] and Ru(III/II).[24,26,27] Figure 3 and Table-S1 will be used to account for modifications to molecular geometries of $[PW_{11}M(H_2O)O_{39}]^{q-}$ [M = Mn(II), Fe(II), Co(II), and Ru(II)], under electrochemical processes. One-electron oxidation of $[PW_{11}Mn(H_2O)O_{39}]^{5-}$ induced constriction of O_{a1}−Mn and O_{b2}−Mn by 0.197 and 0.125 Å, respectively. Oxidation of $[PW_{11}Mn(H_2O)O_{39}]^{5-}$ removes $\sigma^*(O_{a1}$−M) and $\sigma^*(O_{b2}$−M) interactions derived from the overlap of $O2p_x$ or $O2p_y$ orbitals and $d_{x^2-y^2}$ orbitals. One-electron oxidation of $[PW_{11}M(H_2O)O_{39}]^{q-}$ (M = Fe(II) or Ru(II)) had no significant impact to molecular geometry. One-electron oxidation of $[PW_{11}Co(H_2O)O_{39}]^{5-}$ constricted O_c−M by 0.284 Å attributed to the removal of $\sigma^*(O_c$−M) derived from the overlap of $O2p_z$ and d_{z^2} orbital. Herein, $[PW_{11}Co(H_2O)-O_{39}]^{4-}$ possesses the electron configuration: $(d_{xz})^2(d_{yz})^2(d_{xy})^2$ which are (predominantly) non-bonding. Previous work modeling redox processes of POMs have been calculated using the reduction energy (RE) which assumes entropic and

vibrational contributions are negligible.[62] However, the significance of $\sigma^*(O_c$−M), $\sigma^*(O_{a1}$−M), and $\sigma^*(O_{b2}$−M) interactions emphasize the importance of enthalpic, entropic, and zero-point contributions for redox modeling of $[PW_{11}M-(H_2O)O_{39}]^{q-}$ [M = Mn(II) and Co(II)] anions.

Computation of Redox Potentials-Anionic Model. Redox potentials, U^0_{Red} versus SHE, for Mn(III/II), Fe(III/II), Co(III/II), and Ru(III/II) couples present in $[XW_{11}M-(H_2O)O_{39}]^{q-}$; X = As(V), Si(IV), Ge(IV), B(III), and Zn(II) are reported in Figure 4. Computation of U^0_{Red} for $[PW_{11}M-(H_2O)O_{39}]^{q-}$ M = Fe(III/II)/Ru(III/II) closely reproduced the literature within ca. 0.2 V. By contrast, computed values of U^0_{Red} for $[PW_{11}M(H_2O)O_{39}]^{q-}$ M = Mn(III/II)/Co(III/II) were notably underestimated by ca. 0.8—1.0 V. The discrepancy between DFT and experimental potential, U^0_{Error} increased with overall anionic charge of $[XW_{11}M(H_2O)O_{39}]^{q-}$; attributed to the increasing contribution of the self-interaction error. For example, $[ZnW_{11}Mn(H_2O)O_{39}]^{7-/8-}$ produced $U^0_{Error} = 1.26$ V superseding $[PW_{11}Mn(H_2O)O_{39}]^{4-/5-}$ by 0.23 V.

The effect of applied exchange−correlation functional and basis set was assessed for the Mn(III/II), Fe(III/II), Co(III/II), and Ru(III/II) couples in $[PW_{11}M(H_2O)O_{39}]^{q-}$—see Figure 5.
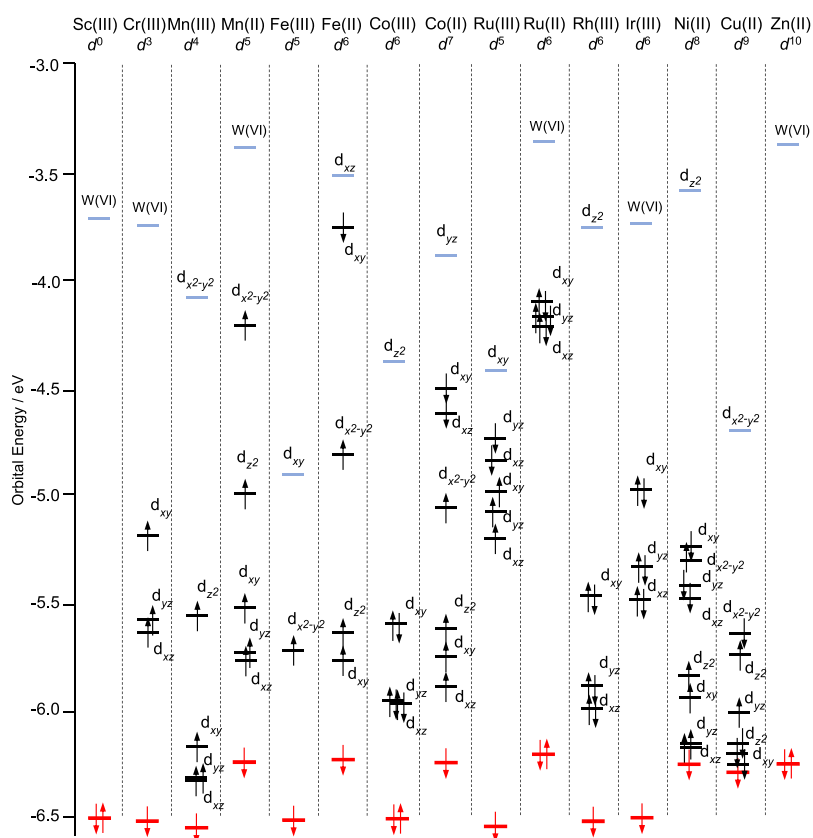
Figure 3. Schematic molecular orbital diagram for $[PW_{11}M(H_2O)O_{39}]^{q-}$ systems, optimized using the PBE/TZP level of theory. Herein, closed shell $[PW_{11}M(H_2O)O_{39}]^{q-}$ systems were computed with the RKS theory—distinguished by spin-paired orbitals. Open shell $[PW_{11}M(H_2O)O_{39}]^{q-}$ systems were computed with UKS theory and are distinguished by separate spin-up and spin-down orbitals. Colors correspond to red = O2(p), blue = W, and black = transition-metal. All orbital energies reported in eV.
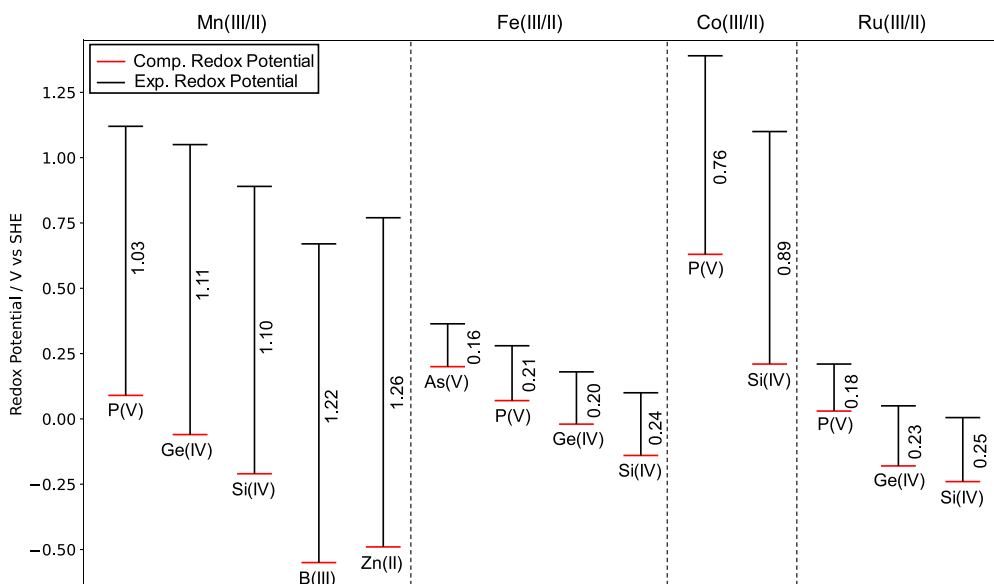

Figure 4. Redox potentials, U^0_{Red} vs SHE, for Mn(III/II), Fe(III/II), Co(III/II), and Ru(III/II) couple present in $[XW_{11}M(H_2O)O_{39}]^{q-}$; X = As(V), Si(IV), Ge(IV), B(III), and Zn(II). All potentials were calculated using the PBE/TZP level of theory. Experimental potentials were obtained from Mn(III/II),[20] Fe(III/II),[21] Co(III/II),[23,24] and Ru(III/II).[24,26,27]

The employment of larger basis sets (TZ2P, QZ4P) proved inferior in reproducing experimental potentials, with respect to triple-ζ + polarization (TZP) basis sets. For example, U^0_{Error} for $[PW_{11}Mn(H_2O)O_{39}]^{q-}$ increased from 1.03 to 1.40 V (ΔU^0_{Error} = 0.37 V) for TZP and QZ4P basis sets, respectively.

Generally, hybrid $x-c$ functionals outperformed GGA methodologies by reducing U^0_{Error} for M(III/II) redox couples. This is evidenced by U^0_{Error} in $[PW_{11}Mn(H_2O)O_{39}]^{q-}$ which notably decreased from 1.03 to 0.28 V (ΔU^0_{Error} = 0.75 V) by incorporating 15% HF exchange (B3LYP*/TZP). However, the
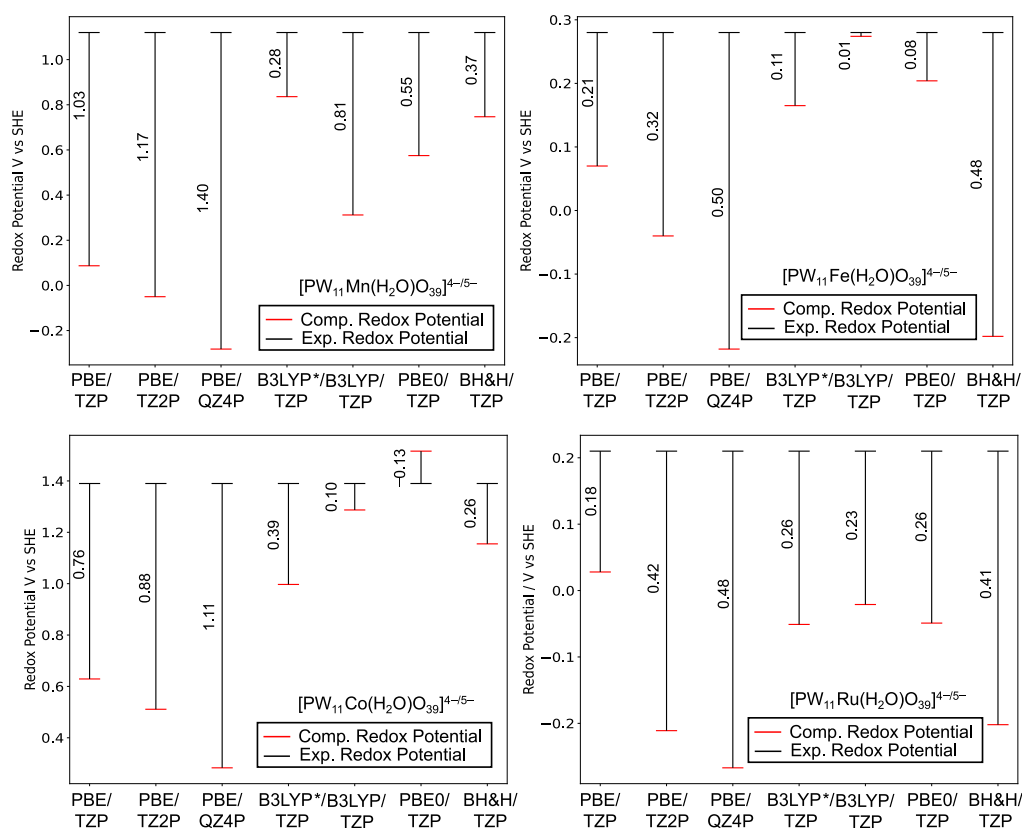
Figure 5. Redox potentials, U^0_{Red} vs SHE, for Mn(III/II), Fe(III/II), Co(III/II), and Ru(III/II) redox couples in $[PW_{11}M(H_2O)O_{39}]^{q-}$. Experimental potentials were obtained from Mn(III/II),[20] Fe(III/II),[21] Co(III/II),[23,24] and Ru(III/II).[24,26,27]

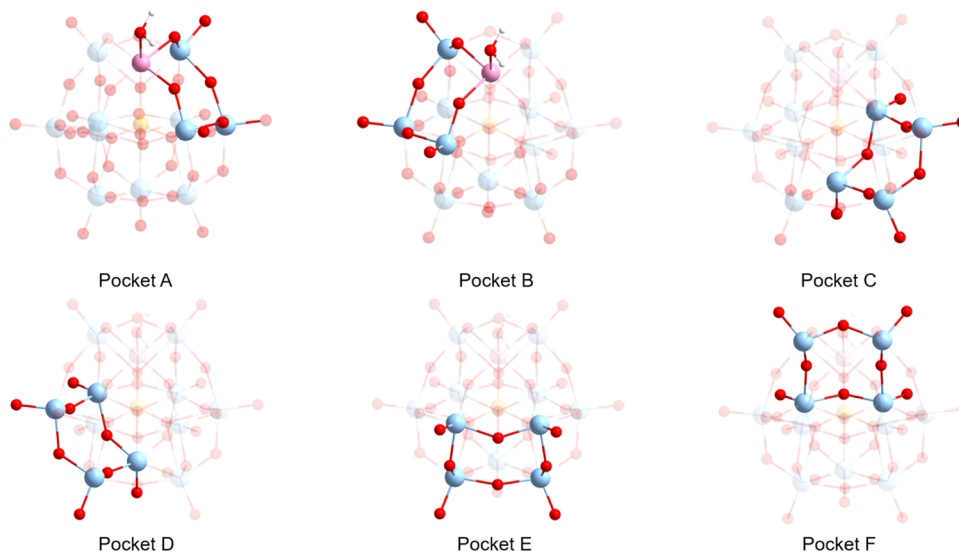**Figure 6.** Schematic representations of 4-fold pockets (A−F) on the surface of $[PW_{11}Co(H_2O)O_{39}]^{5-}$ anions.

optimal $x-c$ functional was not consistent across all M(III/II) couples. For example, Fe(III/II), Co(III/II), and Ru(III/II) couples were optimally reproduced with 20% HF exchange (B3LYP/TZP) calculating U^0_{Error} of 0.01, 0.10, and 0.23 V respectively. Thus far, U^0_{Red} for $[PW_{11}Mn(H_2O)O_{39}]^{q-}$ were calculated without neutralizing their charge, and therefore, large discrepancies associated with the self-interaction error are expected for these calculations. Previous work showed explicitly locating counterions on the surface of the POM, rendering the system charge neutral can reduce this systematic error.[44]

Computation of Redox Potentials-Charge Neutral Model. On the surface of the molecule, the counterion can interact with 4-fold (pocket A−F) or 3-fold pockets—see Figure 6. The 4-fold pockets feature four oxygen atoms capable of interacting with counterions, while 3-fold pockets are comprised three adjacent oxygen atoms which assume a triangular shape. In this work, we concentrated on counterion interactions with the 4-fold pockets, which bind significantly stronger than the 3-fold pockets due to improved Coulomb interactions.

To differentiate between cation arrangements, isomers were identified by their unoccupied pockets. For example, isomer-D corresponds to systems with an absent cation–oxygen interaction at pocket D—see Figure S3. The relative stability of all isomers was evaluated by the difference in electronic energy, E_{Rel}.—see Table 2. ΔE_{Rel} across $K_5[PW_{11}Co(H_2O)O_{39}]$

Table 2. Relative Stability of Cation Arrangements on the Surface of the Keggin $K_x[PW_{11}Co(H_2O)O_{39}]^{q-x}$ (X = 4 or 5) Salts[a]

pocket	E_{Rel}
A	1.105
B	0.941
C	0.373
D	0.000
E	0.323
F	0.001
A,B	1.386
A,C	0.134
A,D	0.000
A,E	0.837
A,F	0.398
B,C	2.111
B,D	2.377
B,E	3.042
B,F	2.550
C,D	1.075
C,E	1.639
C,F	1.211
D,E	1.305
D,F	1.739
E,F	1.650

[a]All energies are reported in kcal mol^{-1}.

isomers were almost negligible at 1.11 kcal mol^{-1}. The discrepancy between pocket A and B was attributed to reduced electrostatic attractive forces because of shielding by the aqua protons, correlating with previous work.[43] Energy differences across $K_4[PW_{11}Co(H_2O)O_{39}]$ isomers were moderate, reporting ΔE_{Rel} of 3.04 kcal mol^{-1}. It is important to recognize the electronic energy difference between the three lowest energy isomers of $K_4[PW_{11}Co(H_2O)O_{39}]$ ranged by >0.4 kcal mol^{-1}. Hence, it is reasonable to assume all arrangements will co-exist in solution. However, for our redox calculations, we focused on the two lowest energy isomers: A and A,D.

Redox potentials, U^0_{Red} versus SHE, for Mn(III/II), Fe(III/II), Co(III/II), and Ru(III/II) couples present in $K_x[XW_{11}M(H_2O)O_{39}]^{q-x}$; X = As(V), Si(IV), Ge(IV), B(III), and Zn(II) are reported in Figure 7. All potentials were calculated using the PBE/TZP level of theory to allow for comparison with the anionic model, shown in Figure 4. The incorporation of counterions positively shifted redox potentials by >500 mV. Computation of U^0_{Red} with $K_x[XW_{11}M(H_2O)O_{39}]^{q-x}$ M = Mn(III/II)/Co(III/II) demonstrated significant improvement, by which U^0_{Error} rarely exceeded 0.50 V. A comparison with Figure 4 shows U^0_{Error} in $K_x[ZnW_{11}Mn(H_2O)O_{39}]^{q-x}$ was reduced from 1.26 to 0.43 V (ΔU^0_{Error} = 0.83 V). However, accuracy in computation of U^0_{Red} for $K_x[XW_{11}M(H_2O)O_{39}]^{q-x}$ M = Fe(III/II)/Ru(III/II) was impaired in which all couples produced U^0_{Error} exceeding 0.35 V.

Thus far, models of $K_x[XW_{11}M(H_2O)O_{39}]^{q-x}$ have employed the A and A,D isomers—see Table 2. Figure 8 reports U^0_{Error} for $K_x[PW_{11}Co(H_2O)O_{39}]^{q-x}$ to assess the sensitivity of our model to different cation arrangements. The current model demonstrated moderate sensitivity across all cation arrangements ranging up to 0.18 V. Comparatively poor agreement with the literature was achieved with the energetically favored A + A,D couples, whose redox couple underestimated potentials by 0.315
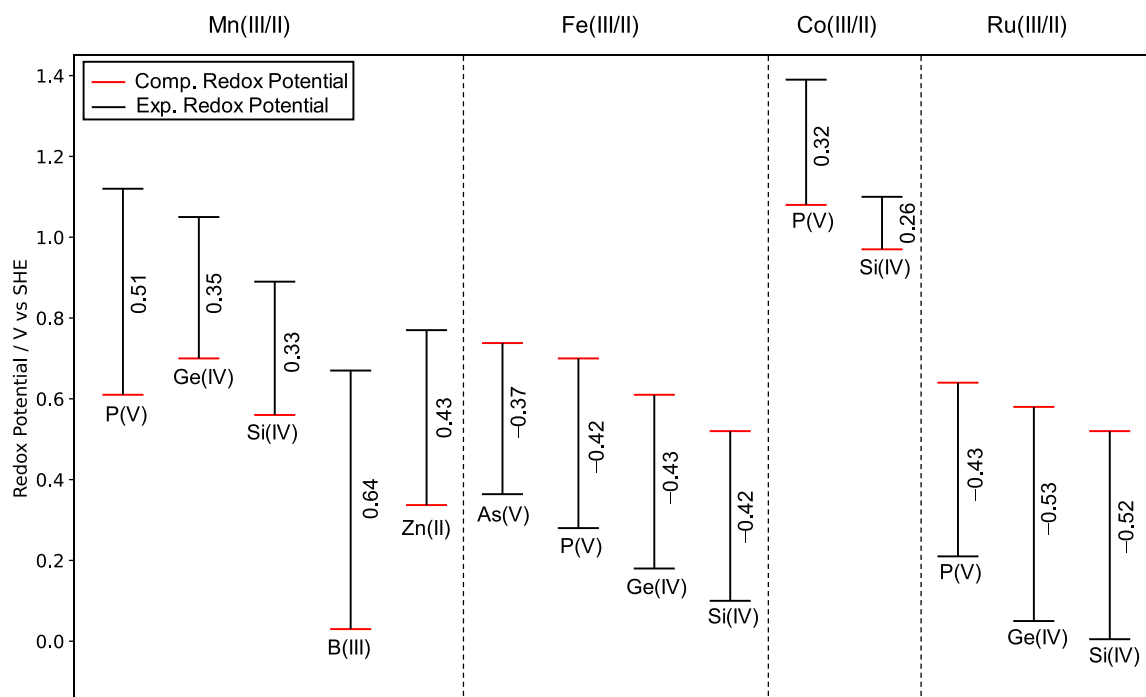
Figure 7. Redox potentials, U^0_{Red} vs SHE, for Mn(III/II), Fe(III/II), Co(III/II), and Ru(III/II) couple present in $K_x[XW_{11}M(H_2O)O_{39}]^{q-x}$; X = P(V), Si(IV), Ge(IV), B(III), and Zn(II). All calculations were performed with the A and A,D cation arrangements. All potentials were calculated using the PBE/TZP level of theory. Experimental potentials were obtained from Mn(III/II),[20] Fe(III/II),[21] Co(III/II),[23,24] and Ru(III/II).[24,26,27]

Figure 8. Redox potentials, U^0_{Red} vs SHE, for all cation rearrangements for $K_x[PW_{11}Co(H_2O)O_{39}]^{q-x}$; $x = 4$ or 5, obtained using the PBE/TZP methodology. Gibbs free energies for all cation arrangements were computed using the zero-point energies and entropic components obtained from GGA−vibrational frequencies for A and A,D isomers. Experimental potentials were obtained from Co(III/II).[23,24]

Figure 9. Redox potentials, U^0_{Red} vs SHE, for Mn(III/II), Fe(III/II), Co(III/II), and Ru(III/II) redox couples in $K_x[PW_{11}M(H_2O)O_{39}]^{q-x}$. All calculations were performed with the A and A,D cation arrangements. Experimental potentials were obtained from Mn(III/II),[20] Fe(III/II),[21] Co(III/II),[23,24] and Ru(III/II).[24,26,27]
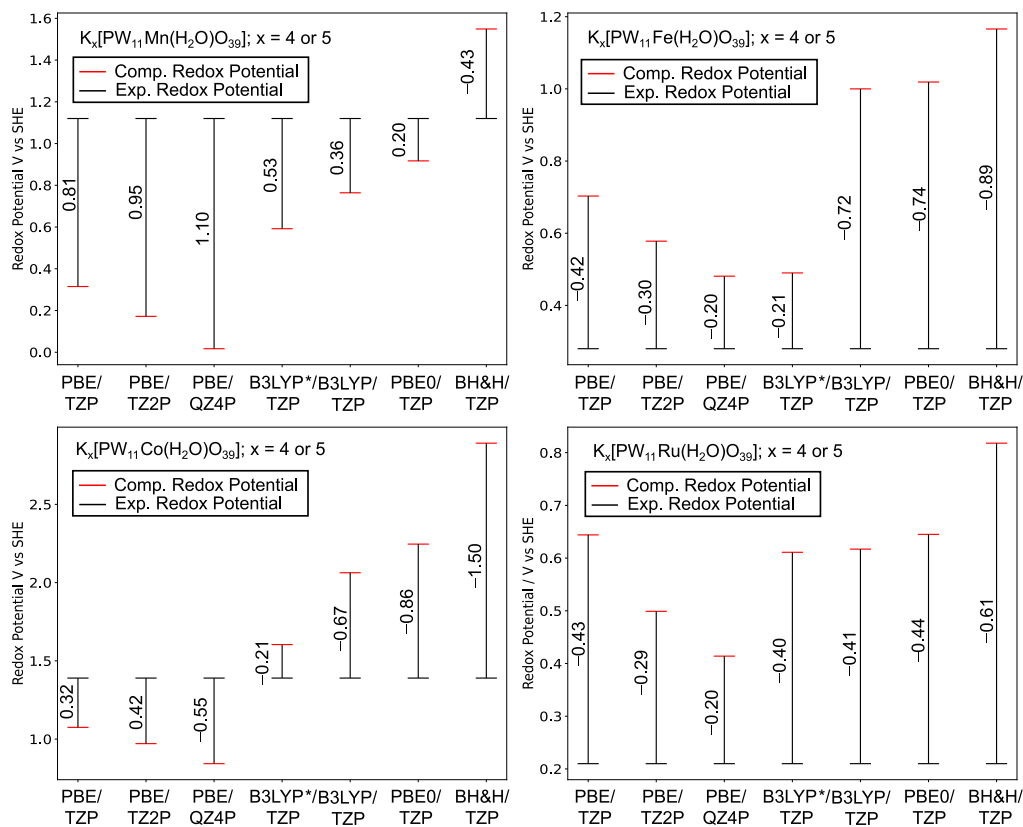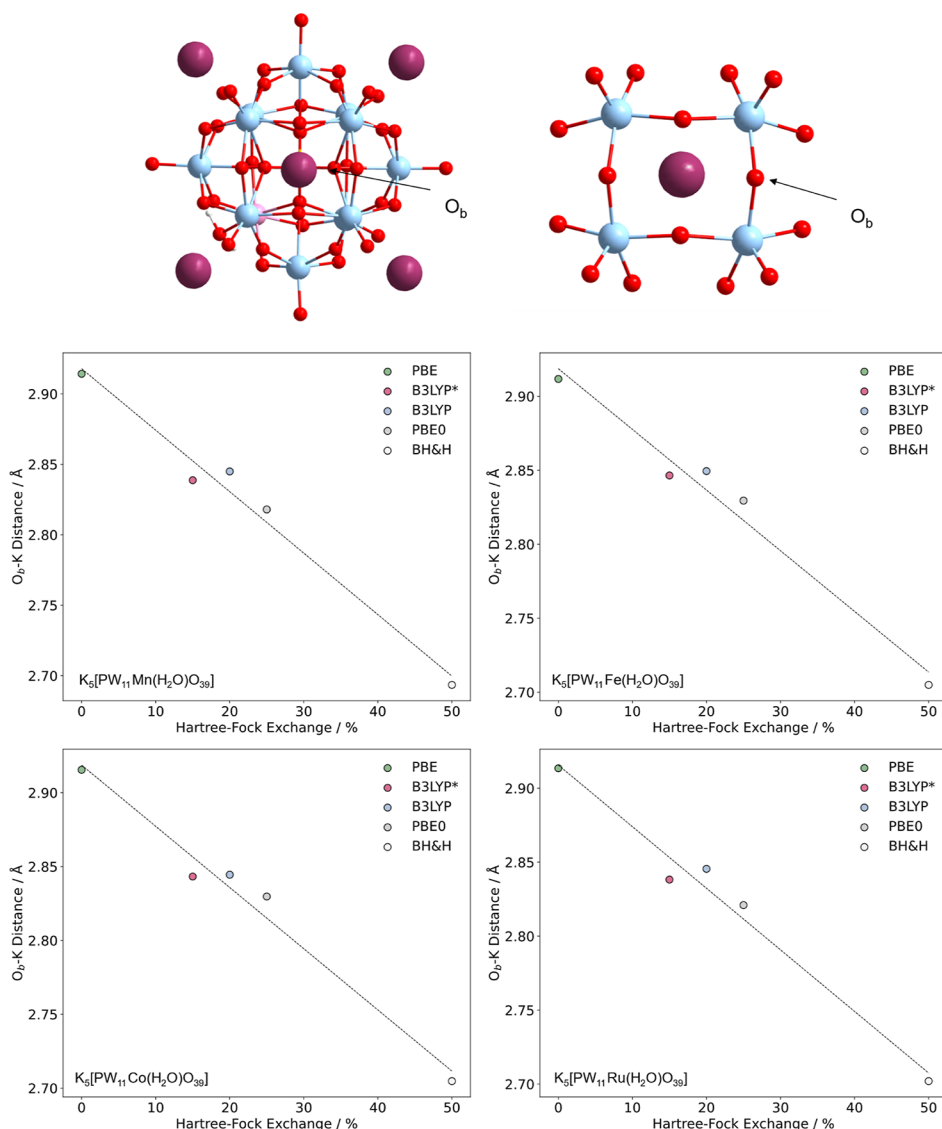
Figure 10. Average counterion−bridging oxygen distance (O_b−K) in $K_5[PW_{11}M(H_2O)O_{39}]$, where M = Mn(II), Fe(II), Co(II), and Ru(II) plotted as a function of HF exchange. All calculations were performed with the A and A,D cation arrangements.

V, with respect to the literature. Accurate computation of U^0_{Red} was achieved with isomers: D + B,E and F + B,E couples, who redox couples underestimated potentials by 0.135 V.

For comparison with Figure 5, we have explored the effect of applied x−c functional and basis set on U^0_{Red} for $K_x[PW_{11}M(H_2O)O_{39}]^{q−x}$ M = Mn(III/II), Fe(III/II), Co(III/II), and Ru(III/II), as shown in Figure 9. The employment of larger basis sets (TZ2P, QZ4P) positively shifted potentials for Mn(III/II) and Co(III/II) couples providing poorer reproduction of the literature, compared to triple-ζ + polarization (TZP) basis sets. This effect was particularly pronounced for $K_x[PW_{11}M(H_2O)O_{39}]^{q−x}$ in which U^0_{Error} increased from 0.35 to 1.07 V (ΔU^0_{Error} = 0.72 V). A comparison with Figure 5 shows incorporation of counterions to $[PW_{11}Mn(H_2O)O_{39}]^{q−}$ reduced U^0_{Error} by 0.68, 0.24, and 0.33 V for TZP, TZ2P, and QZ4P basis sets, respectively.

We have explored the effect of HF exchange on U^0_{Red} for $K_x[PW_{11}M(H_2O)O_{39}]^{q−x}$ M = Mn(III/II), Fe(III/II), Co(III/II), and Ru(III/II). ΔU^0_{Error} using GGA−PBE functional (0% exchange) reflected in the range of 0.32−0.43 V across all redox couples. Those with larger contributions of HF exchange varied

significantly, for example, ΔU^0_{Error} computed using BH&H ranged from 0.43 to 1.50 V. Hybrid functionals exceeding 25% HF exchange did not provide any improvement for reducing ΔU^0_{Error}. As is evident, increasing HF exchange positively shifted U^0_{Red} which was attributed to the over-stabilization of the ion-pairs. Hybrid functionals exceeding 25% HF are not recommended because of large CPU times coupled with significant overestimations to ΔU^0_{Red}.

U^0_{Red} became positively shifted with the increase in contributions of HF exchange. To rationalize this observation, we plotted counterion−bridging oxygen (between pocket D) as a function of HF exchange, see Figure 10. Increasing contributions of HF exchange produced shorter O_b−K distances leading to the over-stabilization of the close contact ion-pairs. The significance of these O_b−K distances is emphasized by the computed range (PBE to BH&H) in O_b−K distances in $K_5[PW_{11}Co(H_2O)O_{39}]$ calculated at ca. 0.2 Å which reflected in ΔU^0_{Red} = 1.29 V. Previous work by Kaledin and co-workers reported the average O_t−K and O_b−K distances for hydrated $[PW_{12}O_{40}][K(H_2O)_{16}]_3$ complexes were 5.1 and 5.7 Å, respectively.[63] To contrast, O_t−K and O_b−K distances in

$K_5[PW_{11}Co(H_2O)O_{39}]$ were ca. 4.1 and 2.8 Å, respectively. Evidently, further improvements should focus on accurately modeling counterion−bridging oxygen distances to enable more accurate computation of U^0_{Red}.

CONCLUSIONS

In this work, we have employed DFT calculations to systematically study the accuracy of various exchange−correlation functionals for reproducing experimental redox properties in mono-transition-metal-substituted Keggin $[XW_{11}M(H_2O)O_{39}]^{q-}$ anions and their corresponding potassium salts. We have focused our attention to Mn(III/II), Fe(III/II), Co(III/II), and Ru(III/II) redox couples associated with $[XW_{11}M(H_2O)O_{39}]^{q-}$ X = P(V), Si(IV), Ge(IV), B(III), and Zn(II). Our aim has been to explore the challenges in computing redox potentials and provide an insight into the geometric and electronic factors controlling it. We employed several $x-c$ functionals including the hybrid class selected by their contributions to HF exchange (15% B3LYP*, 20% B3LYP, 25% PBE0, and 50% BH&H).

For direct comparison, we explicitly located K^+ counterions to render our system charge neutral to reduce systemic discrepancies associated with the self-interaction error. The incorporation of counterions positively shifted redox potentials by >500 mV. By incorporating counterions, significant improvement to U^0_{Red} for Mn(III/II) and Co(III/II) redox couples, in which U^0_{Error} rarely exceeded 0.50 V. This effect was particularly pronounced for U^0_{Error} in $K_x[ZnW_{11}Mn(H_2O)O_{39}]^{q-x}$, whereby U^0_{Error} was reduced from 1.26 to 0.43 V (ΔU^0_{Error} = 0.83 V). However, problems remain as U^0_{Red} for Fe(III/II) and Ru(III/II) were excessively (positively) shifted, attributed to the over-stabilization of the ion-pairs. Previous work has shown the average O_t-K and O_b-K distances for hydrated $[PW_{12}O_{40}][K(H_2O)_{16}]_3$ complexes were 5.1 and 5.7 Å, while our charge neutral model of $K_5[PW_{11}Co(H_2O)O_{39}]$ produced O_t-K and O_b-K distances reporting at ca. 4.1 and 2.8 Å, respectively. We have rationalized this overestimation by plotting O_b-K distances as a function of HF, whereby increasing contributions of exchange (0% PBE to 50% BH&H) produced progressively shorter O_b-K distances. The reported range in O_b-K was only ca. 0.2 Å; however, its significance is highlighted in $K_5[PW_{11}Co(H_2O)O_{39}]$ which reflected in the range of 1.29 V for U^0_{Red}.

Obtaining accurate redox potentials using implicit solvation models remains a challenge. Our results emphasize that understanding the nature of the electrode and electrolyte environment may be essential to obtaining reasonable agreement between theoretical and experimental results. Further improvements to this work by accurately modeling counterion−bridging oxygen distance will enable more accurate computation of U^0_{Red}. The present results emphasis the current approach requires significant improvement to achieve more reliable modeling with respect to experimental work.

ASSOCIATED CONTENT

Ⓢ Supporting Information

The Supporting Information is available free of charge at https://pubs.acs.org/doi/10.1021/acs.inorgchem.3c01115.

Optimized geometries for $[PW_{11}M(H_2O)O_{39}]^{q-}$ and A and A,D isomers of $K_x[PW_{11}M(H_2O)O_{39}]^{q-x}$ (x = 4 or 5); schematic molecular orbital (MO) diagram for Mn(III/II), Fe(III/II), Co(III/II), and Ru(III/II) couples in $[XW_{11}M(H_2O)O_{39}]^{q-}$, where X = As(V), Si(IV), Ge(IV), B(III), and Zn(II); schematic MO for $[PW_{11}M(H_2O)O_{39}]^{q-}$ computed with several $x-c$ functionals; and MO diagrams for $K_x[PW_{11}M(H_2O)O_{39}]^{q-x}$ (x = 4 or 5) obtained from the PBE/TZP level of theory (PDF)

AUTHOR INFORMATION

Corresponding Authors

Rebeca González-Cabaleiro − *Department of Biotechnology, Delft University of Technology, Delft 2628 CD, Netherlands*; Email: R.GonzalezCabaleiro@tudelft.nl

Laia Vilà-Nadal − *School of Chemistry, University of Glasgow, Glasgow G12 8QQ, U.K.*; ⓘ orcid.org/0000-0002-7718-7227; Email: laia.vila-nadal@chem.gla.ac.uk

Author

Jake A. Thompson − *School of Chemistry, University of Glasgow, Glasgow G12 8QQ, U.K.*

Complete contact information is available at:
https://pubs.acs.org/10.1021/acs.inorgchem.3c01115

Author Contributions

L.V.-N. and R.B.-C. conceived the idea together with J.A.T. who designed the modeling approach, performed all the theoretical calculations, and analyzed all the data. J.A.T. wrote the paper and made all the figures in the manuscript with input from L.V. -N and R.B.-C. R.B.-C. and L.V.-N. are equally supervising J.A.T. and corresponding authors in this paper.

Notes

The authors declare no competing financial interest.
The data sets generated using DFT calculations are available in the ioChem-BD database (https://doi.org/10.19061/iochem-bd-6-254).

REFERENCES

(1) Anyushin, A. v.; Kondinski, A.; Parac-Vogt, T. N. Hybrid Polyoxometalates as Post−Functionalization Platforms: From Fundamentals to Emerging Applications. *Chem. Soc. Rev.* **2020**, 49, 382−432.

(2) Gumerova, N. I.; Rompel, A. Polyoxometalates in Solution: Speciation under Spotlight. *Chem. Soc. Rev.* **2020**, 49, 7568−7601.

(3) Izarova, N. v.; Pope, M. T.; Kortz, U. Noble Metals in Polyoxometalates. *Angew. Chem., Int. Ed. Engl.* **2012**, 51, 9492−9510.

(4) Proust, A.; Matt, B.; Villanneau, R.; Guillemot, G.; Gouzerh, P.; Izzet, G. Functionalization and Post−Functionalization: A Step

towards Polyoxometalate−Based Materials. *Chem. Soc. Rev.* **2012**, *41*, 7605−7622.

(5) Vilà-Nadal, L.; Cronin, L. Design and Synthesis of Polyoxometalate−Framework Materials from Cluster Precursors. *Nat. Rev. Mater.* **2017**, *2*, 17054.

(6) Pradeep, C. P.; Long, D. L.; Cronin, L. Cations in Control: Crystal Engineering Polyoxometalate Clusters Using Cation Directed Self−Assembly. *Dalton Trans.* **2010**, *39*, 9443−9457.

(7) Balulla, M. S.; Gamelas, J. A.; Carapuça, H. M.; Cavaleiro, A. M. V.; Schlindwein, W. Electrochemical Behaviour of First Row Transition Metal Substituted Polyoxotungstates: A Comparative Study in Acetonitrile. *Eur. J. Inorg. Chem.* **2004**, 619−628.

(8) Azuma, S.; Kadoguchi, T.; Eguchi, Y.; Hirabaru, H.; Ota, H.; Sadakane, M.; Yanagisawa, K.; Hasegawa, T.; Ueda, T. Metal−Substituted Tungstosulfates with Keggin Structure: Synthesis and Characterization. *Dalton Trans.* **2020**, *49*, 2766−2770.

(9) Liu, R.; Streb, C. Polyoxometalate−Single Atom Catalysts (POM−SACs) in Energy Research and Catalysis. *Adv. Energy Mater.* **2021**, *11*, 2101120.

(10) Murakami, M.; Hong, D.; Suenobu, T.; Yamaguchi, S.; Ogura, T.; Fukuzumi, S. Catalytic Mechanism of Water Oxidation with Single−Site Ruthenium−Heteropolytungstate Complexes. *J. Am. Chem. Soc.* **2011**, *133*, 11605−11613.

(11) Shimoyama, Y.; Ogiwara, N.; Weng, Z.; Uchida, S. Oxygen Evolution Reaction Driven by Charge Transfer from a Cr Complex to Co−Containing Polyoxometalate in a Porous Ionic Crystal. *J. Am. Chem. Soc.* **2022**, *144*, 2980−2986.

(12) Szczepankiewicz, S. H.; Ippolito, C. M.; Santora, B. P.; Van De Ven, T. J.; Ippolito, G. A.; Fronckowiak, L.; Wiatrowski, F.; Power, T.; Kozik, M. Interaction of Carbon Dioxide with Transition−Metal−Substituted Heteropolyanions in Nonpolar Solvents. Spectroscopic Evidence for Complex Formation. *Inorg. Chem.* **1998**, *37*, 4344−4352.

(13) Fabre, B.; Falaise, C.; Cadot, E. Polyoxometalates−Functionalized Electrodes for (Photo)Electrocatalytic Applications: Recent Advances and Prospects. *ACS Catal.* **2022**, *12*, 12055−12091.

(14) González-Cabaleiro, R.; Thompson, J. A.; Vilà-Nadal, L. Looking for Options to Sustainably Fixate Nitrogen. Are Molecular Metal Oxides Catalysts a Viable Avenue? *Front. Chem.* **2021**, *9*, 742565.

(15) Zhang, D.; Zhang, W.; Lin, Z.; Dong, J.; Zhen, N.; Chi, Y.; Hu, C. Mono− And Di−Sc−Substituted Keggin Polyoxometalates: Effective Lewis Acid Catalysts for Nerve Agent Simulant Hydrolysis and Mechanistic Insights. *Inorg. Chem.* **2020**, *59*, 9756−9764.

(16) Kuznetsova, N. I.; Kuznetsova, L. I.; Likholobov, V. A. Catalytic Properties of Cr−Containing Heteropolytungstates in H_2O_2 Participated Reactions: H_2O_2 Decomposition and Oxidation of Unsaturated Hydrocarbons with H_2O_2. *J. Mol. Catal. A: Chem.* **1996**, *108*, 135−143.

(17) Rong, C.; Anson, F. C.; Inorg, F. C. Simplified Preparations and Electrochemical Behavior of Two Chromium−Substituted Heteropolytungstate Anions. *Inorg. Chem.* **1994**, *33*, 1064−1070.

(18) Coronado, E.; Galán-Mascarós, J. R.; Giménez-Saiz, C.; Gómez-García, C. J.; Triki, S. Hybrid Molecular Materials Based upon Magnetic Polyoxometalates and Organic π−Electron Donors: Syntheses, Structures, and Properties of Bis(Ethylenedithio)Tetrathiafulvalene Radical Salts with Monosubstituted Keggin Polyoxoanions. *J. Am. Chem. Soc.* **1998**, *120*, 4671−4681.

(19) Matsuki, Y.; Mouri, Y.; Sakai, Y.; Matsunaga, S.; Nomiya, K. Monomer and Dimer of Mono−Titanium(IV)−Containing α−Keggin Polyoxometalates: Synthesis, Molecular Structures, and Ph−Dependent Monomer−Dimer Interconversion in Solution. *Eur. J. Inorg. Chem.* **2013**, 1754−1761.

(20) Tourné, C. M.; Tourné, G. F.; Malik, S.; Weakley, T. Triheteropolyanions containing copper(II), manganese(II), or manganese(III). *J. Inorg. Nucl. Chem.* **1970**, *32*, 3875−3890.

(21) Toth, J. E.; Anson, F. C. Electrochemical properties of iron (III)−substituted heteropolytungstate anions. *J. Electroanal. Chem.* **1988**, *256*, 361−370.

(22) Shringarpure, P.; Tripuramallu, B. K.; Patel, K.; Patel, A. Synthesis, Structural, and Spectral Characterization of Keggin−Type

Mono Cobalt(II)−Substituted Phosphotungstate. *J. Coord. Chem.* **2011**, *64*, 4016−4028.

(23) Gamelas, J. A. F.; Gaspar, A. R.; Evtuguin, D. V.; Pascoal Neto, C. Transition Metal Substituted Polyoxotungstates for the Oxygen Delignification of Kraft Pulp. *Appl. Catal., A* **2005**, *295*, 134−141.

(24) Rong, C.; Pope, M. T. Lacunary Polyoxometalate Anions Are. Pi.−Acceptor Ligands. Characterization of Some Tungstoruthenate (II, III, IV, V) Heteropolyanions and Their Atom−Transfer Reactivity. *J. Am. Chem. Soc.* **1992**, *114*, 2932−2938.

(25) Sadakane, M.; Rinn, N.; Moroi, S.; Kitatomi, H.; Ozeki, T.; Kurasawa, M.; Itakura, M.; Hayakawa, S.; Kato, K.; Miyamoto, M.; Ogo, S.; Ide, Y.; Sano, T. Preparation and Structural Characterization of Ru^{II}−DMSO and Ru^{III}−DMSO−Substituted α−Keggin−Type Phosphotungstates, $[PW_{11}O_{39}Ru^{II}DMSO]^{5-}$ and $[PW_{11}O_{39}Ru^{III}DMSO]^{4-}$, and Catalytic Activity for Water Oxidation. *Z. Anorg. Allg. Chem.* **2011**, *637*, 1467−1474.

(26) Sadakane, M.; Tsukuma, D.; Dickman, M. H.; Bassil, B.; Kortz, U.; Higashijima, M.; Ueda, W. Structural Characterization of Mono−Ruthenium Substituted Keggin−Type Silicotungstates. *Dalton Trans.* **2006**, 4271−4276.

(27) Ogo, S.; Shimizu, N.; Ozeki, T.; Kobayashi, Y.; Ide, Y.; Sano, T.; Sadakane, M. Determination of α−Keggin Structure of $[GeW_{11}O_{39}Ru^{III}(H_2O)]^{5-}$. Reaction of $[GeW_{11}O_{39}Ru^{III}(H_2O)]^{5-}$ with Dimethyl Sulfoxide to Form $[GeW_{11}O_{39}Ru^{III}(DMSO)]^{5-}$ and Their Structural Characterization. *Dalton Trans.* **2013**, *42*, 2540−2545.

(28) Wei, X.; Bachman, R. E.; Pope, M. T. Rhodium Derivatives of Lacunary Heteropolytungstates Illustrate Metalloporphyrin Analogies. Reductive Dimerization to Rh 2−Linked Keggin Moieties. *J. Am. Chem. Soc.* **1998**, *120*, 10248−10253.

(29) Mukhacheva, A. A.; Volchek, V. v.; Abramov, P. A.; Sokolov, M. N. Blocking ${RhCl}^{2+}$ Disorder in the Crystal Structure of a $[SiW_{11}O_{39}{RhCl}]^{6-}$ Salt: Direct Localization of the Heterometal in a Monosubstituted Keggin Anion. *Inorg. Chem. Commun.* **2018**, *89*, 10−12.

(30) Sokolov, M. N.; Adonin, S. A.; Mainichev, D. A.; Vicent, C.; Zakharchuk, N. F.; Danilenko, A. M.; Fedin, V. P. Synthesis and Characterization of $[PW_{11}O_{39}Ir(H_2O)]^{4-}$: Successful Incorporation of Ir into Polyoxometalate Framework and Study of the Substitutional Lability at the Ir(III) Site. *Chem. Commun.* **2011**, *47*, 7833−7835.

(31) Liu, H.; Gómez-García, C. J.; Peng, J.; Sha, J.; Li, Y.; Yan, Y. 3D−Transition Metal Mono−Substituted Keggin Polyoxotungstate with an Antenna Molecule: Synthesis, Structure and Characterization. *Dalton Trans.* **2008**, 6211−6218.

(32) Qu, L.-Y.; Shan, Q.-J.; Gong, J.; Lu, R.-Q.; Wang, D. R. Synthesis, properties and characterization of Dawson-type tungstophosphate heteropoly complexes substituted by titanium and peroxotitanium†. *J. Chem. Soc., Dalton Trans.* **1997**, 4525−4528.

(33) Lyon, D. K.; Miller, W. K.; Novet, T.; Domaille, P. J.; Evitt, E.; Johnson, D. C.; Finke, R. G. Highly Oxidation Resistant Inorganic−Porphyrin Analogue Polyoxometalate Oxidation Catalysts. 1. The Synthesis and Characterization of Aqueous−Soluble Potassium Salts of α_2−$P_2W_{17}O_{61}(M^{n+}\cdot OH_2)^{(n-10)}$ and Organic Solvent Soluble Tetra−n−Butylammonium Salts of α_2−$P_2W_{17}O_{61}(M^{n+}\cdot Br)^{(n-11)}$ (M = Mn^{3+}, Fe^{3+}, Co^{2+}, Ni^{2+}, Cu^{2+}). *J. Am. Chem. Soc.* **1991**, *113*, 7209−7221.

(34) Weakley, T. J. R. The crystal structures of two heteropolytungstate salts containing anions derived from α−octadecatungstodiphosphate(6−): $(NH_4)_{10}[\alpha_2$−$P_2W_{17}O_{61}]\cdot 8H_2O$ and $(ME_2NH_2)_8[\alpha_2$−$P_2Co(H_2O)W_{17}O_{61}]\cdot 11H_2O$. *Polyhedron* **1987**, *6*, 931−937.

(35) Ogo, S.; Shimizu, N.; Nishiki, K.; Yasuda, N.; Mizuta, T.; Sano, T.; Sadakane, M. Preparation and Redox Studies of α_1− and α_2−Isomers of Mono−Ru−Substituted Dawson−Type Phosphotungstates with a DMSO Ligand: $[\alpha_1/\alpha_2$−$P_2W_{17}O_{61}Ru^{II}(DMSO)]^{8-}$. *Inorg. Chem.* **2014**, *53*, 3526−3539.

(36) Liu, H.; Yue, B.; Sun, W.; Chen, Z.; Jin, S.; Deng, J.; Xie, G.; Shao, Q.; Wu, T. Synthesis and Characterization of Noble−Metal−Substituted Daw−Son−Type Polyoxometalates. *Transit. Met. Chem.* **1997**, *22*, 321−325.

(37) Bartis, J.; Kunina, Y.; Blumenstein, M.; Francesconi, L. C. Preparation and Tungsten−183 NMR Characterization of [α−1−

$P_2W_{17}O_{61}]^{10-}$, $[\alpha-1-Zn(H_2O)P_2W_{17}O_{61}]^{8-}$, and $[\alpha-2-Zn(H_2O)-P_2W_{17}O_{61}]^{8-}$. *Inorg. Chem.* **1996**, *35*, 1497−1501.

(38) Misra, A.; Kozma, K.; Streb, C.; Nyman, M. Beyond Charge Balance: Counter-Cations in Polyoxometalate Chemistry. *Angew. Chem., Int. Ed.* **2020**, *59*, 596−612.

(39) López, X.; Maestre, J. M.; Bo, C.; Poblet, J. M. Electronic Properties of Polyoxometalates: A DFT Study of $\alpha/\beta-[XM_{12}O_{40}]^{n-}$ Relative Stability (M=W, Mo and X a Main Group Element). *J. Am. Chem. Soc.* **2001**, *123*, 9571−9576.

(40) Zhang, F. Q.; Wu, H. S.; Qin, X. F.; Li, Y. W.; Jiao, H. On the $\alpha/\beta-[AlW_{12}O_{40}]^{5-}$ Stability: Revisited. *J. Mol. Struct.: THEOCHEM* **2005**, *755*, 113−117.

(41) Aparicio, P. A.; López, X.; Poblet, J. M. Ability of DFT calculations to correctly describe redox potentials and electron (de)localization in polyoxometalates. *J. Mol. Eng. Mater.* **2014**, *02*, 1440004.

(42) Aparicio, P. A.; Poblet, J. M.; Lõpez, X. Tungsten Redox Waves in $[XMW_{11}O_{40}]^{n-}$ (X = P, Si, Al and M = W, Mo, V, Nb, Ti) Keggin Compounds − Effect of Localised/Delocalised Charges. *Eur. J. Inorg. Chem.* **2013**, 1910−1916.

(43) Kremleva, A.; Aparicio, P. A.; Genest, A.; Rösch, N. Quantum Chemical Modeling of Tri−Mn−Substituted W−Based Keggin Polyoxoanions. *Electrochim. Acta* **2017**, *231*, 659−669.

(44) Kremleva, A.; Rösch, N. Modeling the Effect of the Electrolyte on Standard Reduction Potentials of Polyoxometalates. *J. Phys. Chem. C* **2018**, *122*, 18545−18553.

(45) Falbo, E.; Penfold, T. J. Redox Potentials of Polyoxometalates from an Implicit Solvent Model and QM/MM Molecular Dynamics. *J. Phys. Chem. C* **2020**, *124*, 15045−15056.

(46) Santos, F. M.; Brandão, P.; Félix, V.; Nogueira, H. I. S.; Cavaleiro, A. M. V. Synthesis and Properties of New Materials with Cobalt(II), Iron(III) and Manganese(III)−Substituted Keggin Polyoxotungstates and 1−Alkyl−3−Methylimidazolium Cations. *Polyhedron* **2015**, *101*, 109−117.

(47) te Velde, G.; Bickelhaupt, F. M.; Baerends, E. J.; Fonseca Guerra, C.; van Gisbergen, S. J. A.; Snijders, J. G.; Ziegler, T. Chemistry with ADF. *J. Comput. Chem.* **2001**, *22*, 931−967.

(48) Perdew, J. P.; Burke, K.; Ernzerhof, M. Generalized Gradient Approximation Made Simple. *Phys. Rev. Lett.* **1996**, *77*, 3865−3868.

(49) Burke, K.; Perdew, J. P.; Wang, Y. Derivation of a Generalized Gradient Approximation: The PW91 Density Functional. *Electronic Density Functional Theory: Recent Progress and New Directions*; Plenum Press, 1998; pp 81−111.

(50) Becke, A. D. Density−Functional Exchange−Energy Approximation with Correct Asymptotic Behavior. *Phys. Rev. A* **1988**, *38*, 3098−3100.

(51) Perdew, J. P. Density−Functional Approximation for the Correlation Energy of the Inhomogeneous Electron Gas. *Phys. Rev. B: Condens. Matter Mater. Phys.* **1986**, *33*, 8822−8824.

(52) Reiher, M.; Salomon, O.; Artur Hess, B. Reparameterization of Hybrid Functionals Based on Energy Differences of States of Different Multiplicity. *Theor. Chem. Acc.* **2001**, *107*, 48−55.

(53) Lee, C.; Yang, W.; Parr, R. G. Development of the Colle-Salvetti correlation-energy formula into a functional of the electron density. *Phys. Rev. B: Condens. Matter Mater. Phys.* **1988**, *37*, 785−789.

(54) Ernzerhof, M.; Scuseria, G. E. Assessment of the Perdew−Burke−Ernzerhof Exchange−Correlation Functional. *J. Chem. Phys.* **1999**, *110*, 5029−5036.

(55) Becke, A. D. A new mixing of Hartree−Fock and local density-functional theories. *J. Chem. Phys.* **1993**, *98*, 1372−1377.

(56) Chai, J.-D.; Head-Gordon, M. Systematic Optimization of Long−Range Corrected Hybrid Density Functionals. *Phys. Chem. Chem. Phys.* **2008**, *128*, 084106.

(57) Sure, R.; Brandenburg, J. G.; Grimme, S. Small Atomic Orbital Basis Set First−Principles Quantum Chemical Methods for Large Molecular and Periodic Systems: A Critical Analysis of Error Sources. *ChemistryOpen* **2016**, *5*, 94−109.

(58) Van Lenthe, E.; Baerends, E. J. Optimized Slater−Type Basis Sets for the Elements 1−118. *J. Comput. Chem.* **2003**, *24*, 1142−1156.

(59) Van Lenthe, E.; Ehlers, A.; Baerends, E. J. Geometry Optimizations in the Zero Order Regular Approximation for Relativistic Effects. *J. Chem. Phys.* **1999**, *110*, 8943−8953.

(60) Pye, C. C.; Ziegler, T. An implementation of the conductor-like screening model of solvation within the Amsterdam density functional package. *Theor. Chem. Accounts Theor. Comput. Model.* **1999**, *101*, 396−408.

(61) Truhlar, D. G.; Cramer, C. J.; Lewis, A.; Bumpus, J. A. Molecular Modeling of Environmentally Important Processes: Reduction Potentials. *J. Chem. Educ.* **2004**, *81*, 596.

(62) Busche, C.; Vilà-Nadal, L.; Yan, J.; Miras, H. N.; Long, D. L.; Georgiev, V. P.; Asenov, A.; Pedersen, R. H.; Gadegaard, N.; Mirza, M. M.; Paul, D. J.; Poblet, J. M.; Cronin, L. Design and Fabrication of Memory Devices Based on Nanoscale Polyoxometalate Clusters. *Nature* **2014**, *515*, 545−549.

(63) Kaledin, A. L.; Yin, Q.; Hill, C. L.; Lian, T.; Musaev, D. G. Ion−Pairing in Polyoxometalate Chemistry: Impact of Fully Hydrated Alkali Metal Cations on Properties of the Keggin $[PW_{12}O_{40}]^{3-}$Anion. *Dalton Trans.* **2020**, *49*, 11170−11178.